

MUON LIFETIME MEASUREMENT

Antonellini Ilaria, Blasi Toccaceli Maria, Bonali Elena, Pasquini Simone

3, 24, 29 April 2025

1 Abstract

The goal of the experiment is to measure the lifetime of cosmic ray muons. To achieve this, a detector consisting of three scintillator planes equipped with photomultiplier tubes and an iron block capable of stopping muons was used. The lifetime was estimated by acquiring two samples of data using two different configurations: one with the iron block between the last two scintillators and one without it. In particular, the muon lifetime estimated from the first dataset is $\tau_{0,1} = (2.104 \pm 0.060) \mu s$ while, from the combination of the two different sets of data, the lifetime of muons stopping in iron and emitting an upward electron – representing the 68.5% of the total upgoing events – is estimated to be $\tau_{0,2} = (2.09 \pm 0.16) \mu s$. Estimates of the muon capture rate in iron were also obtained, yielding $\tau_{c,1} = (0.343 \pm 0.044) \mu s$ and $\tau_{c,2} = (0.231 \pm 0.097) \mu s$. While the muon lifetime $\tau_{0,1}$ and the capture rate $\tau_{c,1}$ obtained from the first dataset are not compatible with the expected theoretical values, the estimates from the second dataset, $\tau_{0,2}$ and $\tau_{c,2}$, show compatibility within uncertainties.

2 Introduction

The muon is a fundamental charged lepton characterized by a mass of approximately 106 MeV [2] and a mean lifetime of $\tau_0 = (2196980.3 \pm 2.2) \text{ ps}$ [1]. Cosmic ray muons are generated in the upper atmosphere as decay products of hadronic showers, which are caused by the interaction between primary cosmic rays and atmospheric nuclei. Specifically, primary cosmic rays interact with protons (hydrogen nuclei) in approximately 89% of cases, while interactions with other nuclei – mostly helium, carbon and oxygen – account for the remaining fraction, as shown in Eq. 1.

$$\text{CR} + \text{N} \rightarrow \pi^\pm, K^\pm, \pi^0, K^0 \dots \quad (1)$$

These interactions lead to the production of mesons, mainly pions and kaons, which further decay into muons. Originating in the upper atmosphere at altitudes around 15 km, these muons travel at nearly the speed of light, reaching sea level in approximately 50 μs . Due to relativistic time dilation, a significant portion of muons does not decay before reaching the Earth's surface, allowing for their detection. The muon energy at sea level is generally $\gtrsim 1 \text{ GeV}$ and their flux is $\sim 1 \text{ cm}^{-2} \text{ s}^{-1}$. Positive and negative muons decay as:

$$\mu^+ \rightarrow e^+ \nu_e \bar{\nu}_\mu, \quad \mu^- \rightarrow e^- \bar{\nu}_e \nu_\mu. \quad (2)$$

Moreover, while μ^+ only undergo decay, μ^- may either decay or be captured by the electric field of a nucleus:

$$\mu^- + p \rightarrow n + \nu_\mu. \quad (3)$$

The muon decay law in its rest frame is described by:

$$N(t) = N(0)e^{-\frac{t}{\tau}}, \quad (4)$$

where $N(t)$ is the number of muons at time t , $N(0)$ is the initial number of muons and τ is the mean muon lifetime. For μ^- , τ is the result of the competition between decay τ_0 and capture τ_c , and can be expressed as:

$$\frac{1}{\tau} = \frac{Q}{\tau_0} + \frac{1}{\tau_c}, \quad (5)$$

where Q is the Huff factor, which accounts for the slight decrease in available energy when the muon is in a bound state, and $1/\tau_c = 44.0 \cdot 10^5 \text{ s}^{-1}$ for iron [3]. Contrary to μ^- , the τ of μ^+ just considers decay and has essentially the same value as τ_0 . As a result, the total decay rate of both μ^+ and μ^- muons can be expressed as:

$$N(t) = N(\mu^-, 0)e^{-\frac{t}{\tau_0}}e^{-\frac{t}{\tau_c}} + N(\mu^+, 0)e^{-\frac{t}{\tau_0}}. \quad (6)$$

By introducing the atmospheric muon charge ratio:

$$R = \frac{N(\mu^+)}{N(\mu^-)}, \quad (7)$$

which at the Earth's surface is within the range $[1.1, 1.2]$ [3], the muon decay rate in Eq. 6 can be redefined as:

$$N(t) = N(\mu^+, 0)e^{-\frac{t}{\tau_0}} \left(1 + \frac{1}{R}e^{-\frac{t}{\tau_c}} \right). \quad (8)$$

The goal of the experiment is to measure the lifetime of cosmic ray muons. To achieve this, two different setups were built, providing a large sample of muon decay times.

3 Experimental setup and development

The main components used for the experimental setup are:

- a detector, consisting of three scintillator planes, each coupled to two photomultiplier tubes (PMTs), and an iron block;
- a Nuclear Instrumentation Module (NIM) electronics, including:
 - CAEN High Voltage (HV) power supply remotely controlled via the GECO application;
 - a CAEN N625 quad linear FAN-IN-FAN-OUT module, used to replicate a signal up to four times;
 - a CAEN N840 discriminator, used to convert an input analog signal into an output logical signal when a fixed threshold is exceeded;
 - a CAEN N108A dual delay, able to introduce precise time delays to signals;
 - a CAEN N93B dual timer which can generate precise time delays;
 - a CAEN N455 quad coincidence logic unit and a CAEN N405 3-fold logic unit performing the logic functions selected;
 - a CAEN N1145 quad scaler and preset counter/timer employed for counting pulses for a user defined time interval;
- a TELEDYNE T3DSO1104 digital storage oscilloscope;

- a CMOD-S7 Field Programmable Gate Array (FPGA) board, used for time interval measurement and readout;
- a computer, used for data storage and analysis.

3.1 Preliminary setup and characterization of the detector

During the first laboratory session, the scintillator plane connected to PMTs labeled as 3 and 4 was characterized. In particular, the optimal values for both HV supply and PMTs' thresholds were found, along with an estimate of the muon detection efficiency.

The scintillator planes are enclosed in aluminum boxes featuring three electrical connections on one side: one HV, powering the two PMTs in parallel, and two LEMO cables, used as electronic connectors for the PMT signal outputs. Inside the aluminum box there are two scintillator tiles ($\sim 580 \text{ cm}^2$ each) joined together, wavelength shifting (WLS) fibers running along the joint and two PMTs at both ends of the fibers. The PMTs' model is Hamamatsu H316504 and their nominal working voltage is around 1000 V.

Firstly, to determine the optimal HV supply value, a logic circuit was built using an initial threshold guess of 20 mV. A second scintillator plane, equipped with PMTs labeled 11 and 12 (operated at an HV of 1000 V and with a threshold of 20 mV), was used as a reference and placed below the plane under test. Four channels of the scaler were used to record the individual number of events given by the two PMTs under test (3 and 4), as well as the two number of coincidence events between each PMT under test and the reference plane, the latter defined by the coincidence of its PMTs (11 and 12). Measurements were taken in fixed time intervals of 100 s at HV values ranging from 700 V to 1150 V, in increments of 50 V.

The selected HV value (see Sec. 4.1) was then set as the best working value for powering the two PMTs under test. Moreover, the threshold voltage of the reference plane was fixed at 2 mV in order to execute the threshold scan of the scintillator under test, using the same logic circuit as before. The threshold settings were varied through the discriminator in increments of 10 mV, starting from 2 mV up to 90 mV. At each threshold setting, the scaler counted the number of detected events in fixed time intervals of 100 s.

Finally, the efficiency of the scintillator under test was measured employing two reference scintillator planes, the one with PMTs labeled as 11 and 12 (with 98.3% efficiency) and another one with PMTs labeled as 9 and 10 (with 98.8% efficiency), both operating at an HV of 1000 V and with a threshold of 20 mV. To compute the efficiency, the scintillator under test was placed between the two reference scintillators. A new logic circuit was built in order to measure the number of coincidence events between the three planes (where each one is the coincidence of its two PMTs) and the coincidence events between the two reference planes; the acquisition lasted 1000 s and the efficiency was calculated as the ratio between the former and the latter number of events.

3.2 Data acquisition setup

During the second laboratory shift, the setup for the data acquisition was prepared. The configuration consisted of three scintillator planes, each connected with two PMTs as explained in Sec. 3.1, and an absorber layer composed of two iron slabs with a total thickness of 1 cm. In the experimental setup, illustrated in Fig. 1, two scintillator planes were placed above the absorber, separated by a $(2.7 \pm 0.1) \text{ cm}$ spacer to geometrically constrain muon tracks, while the third scintillator was put under the absorber. The analog signals coming from the PMTs, if above the threshold values set for each of them, were converted into digital signals by the discriminator

module. For each scintillator plane, the signals from the two associated PMTs were combined using a logical AND to reduce the noise. These logical operations were performed with the quad coincidence logic unit, after connecting the PMTs with LEMO cables.

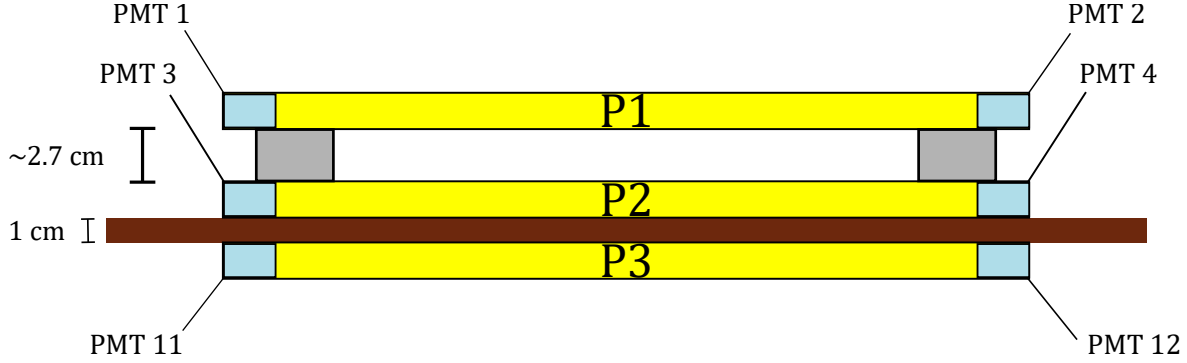


Figure 1: Data acquisition setup. From top to bottom: two scintillator planes, each coupled with two PMTs, separated by two spacers, the iron absorber layer and the third scintillator with its PMTs.

To power the PMTs, each scintillator was connected to an HV channel set to the characteristic working points. HV and threshold values for each scintillator are indicated in Tab. 1.

Scintillator plane	PMTs	HV (V)	Threshold (mV)
P1	1–2	1100	60
P2	3–4	1050	30
P3	11–12	1000	30

Table 1: Operating parameters of the scintillator planes: HV and threshold.

To properly select muon decay events, the trigger logic shown in Fig. 2 was set up. The trigger required a coincidence (logical AND) between the signals from the two scintillators placed above the absorber - indicating a muon passing through them - and the absence of a signal from the scintillator below the absorber, implemented using a logical NOT. This implementation aimed to activate the trigger whenever a muon stops before or within the absorber and to exclude signals produced by muons crossing all three scintillators. These logical operations were performed with the 3-fold logic unit, after connecting the discriminated output of each scintillator to this part of the crate via LEMO cables.

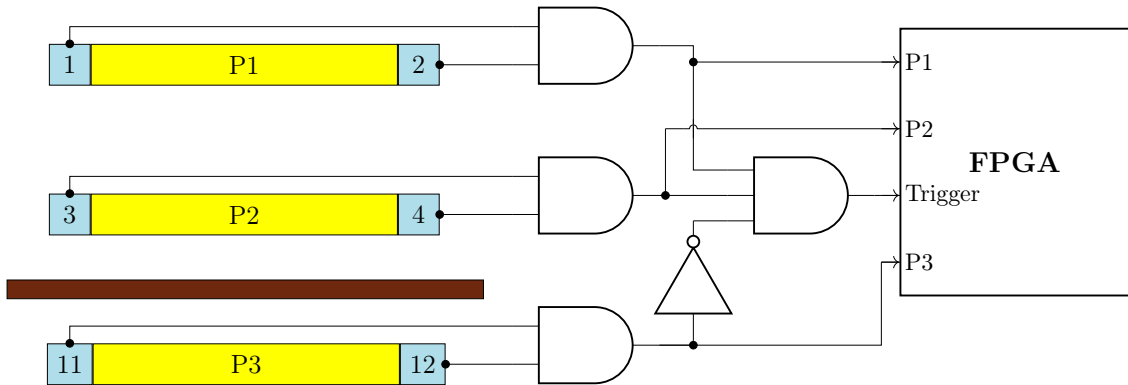


Figure 2: Trigger logic implementation and scheme of the logic circuit reading the signals from the scintillators and transmitting them to the FPGA. In this picture are not represented the modules dedicated to the ADC and the delay.

To ensure an efficient veto by P3 signal, its width was increased using the dedicated setting at the coincidence unit output, while signals from P1 and P2 were delayed using the dual delay module. The width of the signal of P3 was set to ~ 300 ns and the delay on the signals of P1 and P2 with respect to the signal of P3 was set to ~ 70 ns.

The signals given by P1, P2, P3 and the trigger were sent via LEMO cables to a FPGA board, as shown in Fig. 2. The FPGA board was programmed to record data through its connection with the computer. To correctly store data, the incoming NIM logic signals needed to be firstly converted into the LVDS (Low Voltage Differential Signaling) format. Once converted, the signals were processed by a measurement unit on the FPGA. Here, the trigger transition from a logical 0 to a logical 1 generates a start signal that activates the counter inside the FPGA, if it was not already enabled by a previous trigger transition. After its activation, the counter always runs until its maximum value is reached, which corresponds to $16 \mu\text{s}$. The counter is connected to three 12-bits registers, one for each scintillator plane, all initialized with the hexadecimal value FFF and already enabled. When a plane signal is detected, i.e. a possible electron signal is produced, the register loads the counter value and it is disabled from further writings. As soon as the counter reaches its maximum value, data stored on the registers is transmitted to the computer. Finally, the value of the registers is recorded on a text file. The data acquisition lasted for 427919 s.

To ensure a proper conversion between the number of counts provided by the FPGA and a time measurement, the FPGA was carefully calibrated through the dual timer module. This latter was set to generate a constant rate of pulses separated by a fixed time interval. These periodic pulses were outputted by the END MARKER 1 channel. An analogous constant rate of pulses was produced by the END MARKER 2, delayed with respect to the previous one. The signal given by the END MARKER 1 simulates a muon stop event, while the one from END MARKER 2 an electron event. Eight different values for the delay of signals from END MARKER 2 were chosen and measured using the oscilloscope. For each delay value, about 1000 FPGA events were recorded for analysis.

To pass the simulated signals to the FPGA, a dedicated logic circuit was implemented. This circuit was designed to replicate the trigger condition illustrated in Fig. 2, this time based on the simulated events. While its overall structure closely mirrors that of Fig. 2, a crucial modification was made: the first-level AND gate was replaced with an OR gate, as shown in Fig. 3.

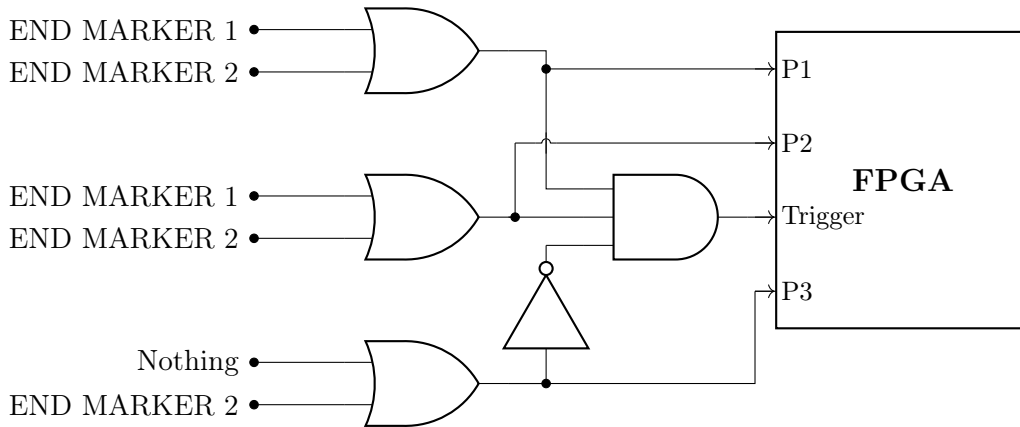


Figure 3: Scheme of the logic circuit reading the simulated signals from END MARKER 1 and END MARKER 2, used to calibrate the FPGA.

3.3 Data acquisition setup without the absorber

During the third laboratory shift, the experimental setup used for the previous data acquisition was slightly modified, in order to estimate the number of muons decaying in the second scintillator. To achieve this, the iron layer was removed. The modified setup consisted of three scintillator planes one above the other as in the previous setup, with P1 and P2 that were separated by the same (2.7 ± 0.1) cm spacer, as seen in Sec. 3.2. In addition, a spacer of the same height of the iron layer was inserted between P2 and P3 to ensure the same geometrical acceptance of the previous configuration. The illustration of the new experimental setup is shown in Fig. 4. The trigger condition remained unchanged from the previous data acquisition, as the circuit programmed in the FPGA. This data acquisition lasted for 762697 s.

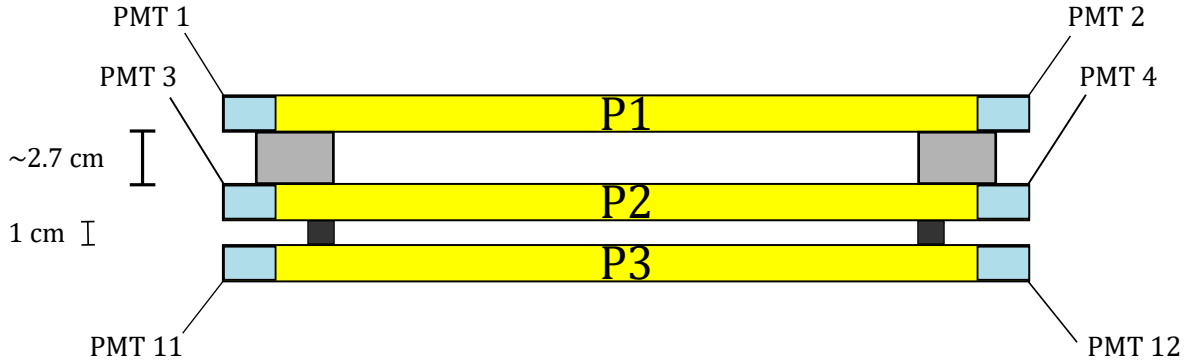


Figure 4: Data acquisition setup for the estimation of the muons decaying in the second scintillator. From top to bottom: three scintillator planes coupled to two PMTs each.

4 Results and discussion

4.1 Analysis of the characterization of the detector

Fig. 5 shows the rate of each PMT coupled to the scintillator under test (PMTs 3-4) as a function of the applied HV, revealing the expected exponential increase. However, this measurement does not allow us to determine the optimal HV supply value since it provides no indications about the capability of these PMTs to discriminate between physical signals and noise or dark counts.

More information can be obtained by plotting the coincidence rates between each PMT and a reference plane as a function of the HV, since noise or dark counts are very unlikely to produce accidental coincidences between different planes. Indeed, as shown in Fig. 6, the coincidence determines the existence of an HV region at which the coincidence rate for both PMTs stops increasing and flattens into a plateau, contrary to Fig. 5. This plateau corresponds to the actual rate of muons crossing both scintillator planes. The HV value at the onset of the plateau represents the optimal working point of the scintillator under test, where both PMTs achieve full detection efficiency while maintaining a low rate of dark counts. The optimal value extrapolated from Fig. 6 is 1050 V.

The plot shown in Fig. 7 displays the threshold scan obtained for the scintillator under test. The observed trend results from the superposition of noise and an ideal muon signal. The former is assumed to follow an exponential distribution, the latter takes on a constant value up to the point where the threshold exceeds its amplitude. From Fig. 7 the threshold value to be set on the discriminator is chosen to be 30 mV, as this value is sufficiently above the noise level to minimize false triggers, while still being low enough to ensure the detection of physical signals.

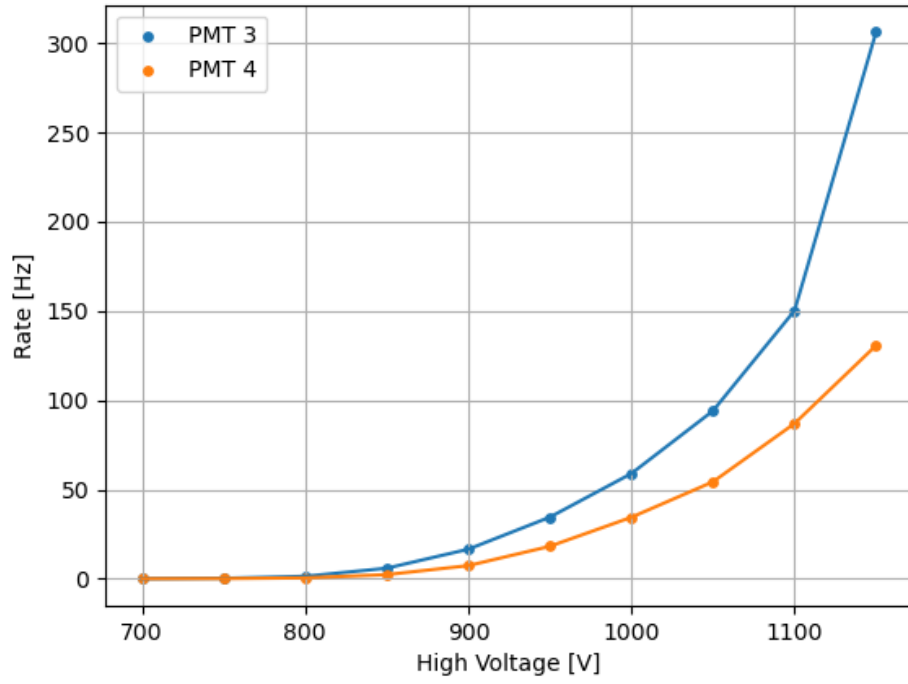


Figure 5: Rates of PMTs 3 and 4 as a function of the HV.

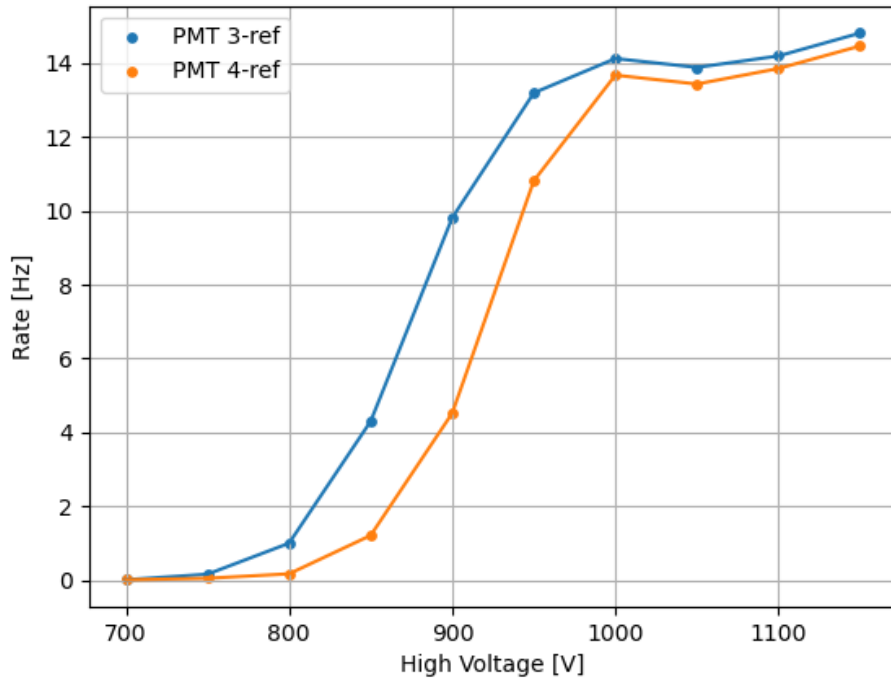


Figure 6: Coincidence rates of PMTs 3 and 4 and a reference plane as a function of the HV.

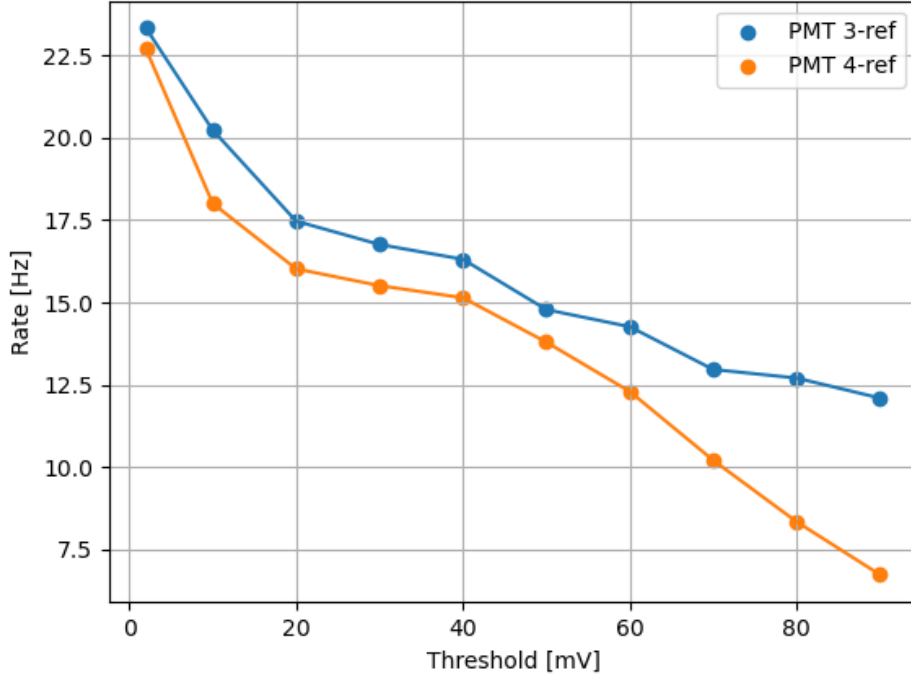


Figure 7: Threshold scan obtained by counting the coincidence rates of PMTs 3 and 4 and a reference plane for different threshold values.

During the efficiency calculation of the scintillator under test, lasted 1000 s, the coincidence condition on the three scintillators yielded $(1228 \pm 11) \cdot 10$ events, while the one involving the two reference scintillators provided $(1278 \pm 11) \cdot 10$ events. Consequently, the calculated efficiency is $0.9606^{+0.0033}_{-0.0035}$ with a confidence level of 95%.

4.2 FPGA calibration

Following the procedure described in Section 3.2, eight data files were obtained, each containing approximately 1400 events. Each file includes time measurements provided by the FPGA, related to a fixed delay of signals from END MARKER 2 with respect to END MARKER 1, which have to be compared with the corresponding time interval measured through the oscilloscope in order to properly calibrate the FPGA. For each file, an average value was calculated.¹ These averages were plotted as a function of the corresponding oscilloscope time, as shown in Fig. 8. A linear fit of the form $y = mx + q$ was then performed over the histogram, where y represents the number of FPGA counts and x the times measured by the oscilloscope. The inverse of the slope extrapolated from this fit corresponds to the conversion factor from FPGA counts to actual time measurements. Specifically, the value of the conversion factor is:

$$(4.0005 \pm 0.0011) \text{ ns.} \quad (9)$$

Moreover, since the trigger signal that starts the FPGA's internal counter is delayed with respect to the END MARKER 1 signals sent to the oscilloscope, a time offset is introduced between the

¹The average value for each data file was computed using a profile histogram, created with the TProfile class provided by ROOT.

measurements provided by the two devices. This time offset can be estimated by considering the intercept of the fit function with the x-axis. The estimated value of the time offset is:

$$(109.1 \pm 1.8) \text{ ns.} \quad (10)$$

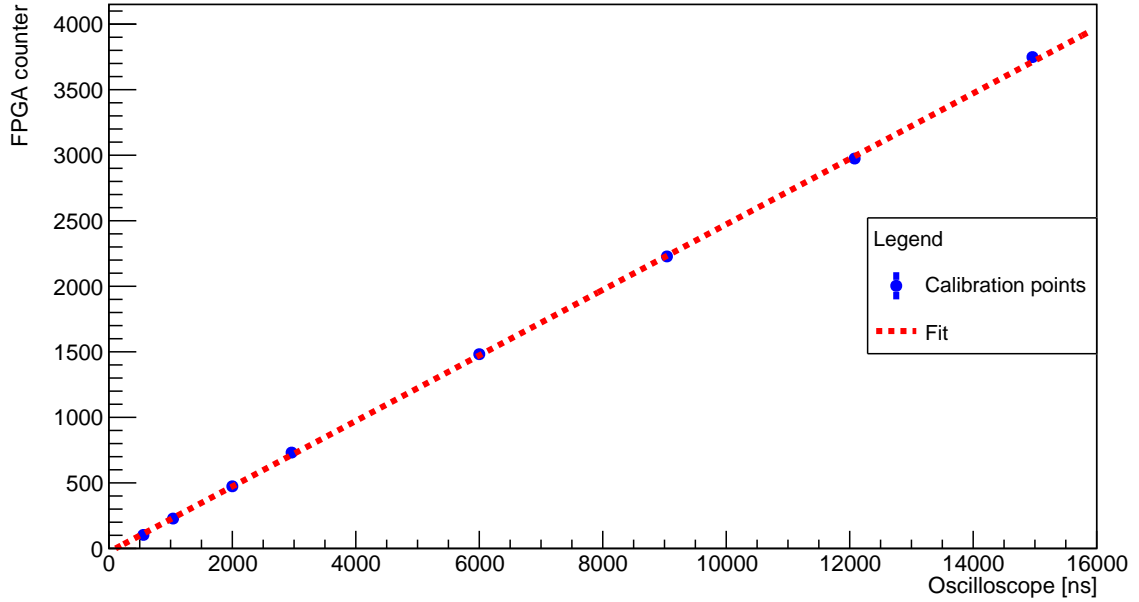


Figure 8: Average value of each data file provided by the FPGA plotted as a function of the corresponding time measured by the oscilloscope.

4.3 Muon lifetime

Once the conversion factor and time offset were determined, all data collected during the first acquisition were converted into time measurements and used to generate histograms. The one shown in Fig. 9 includes all detected electron events. Subsequently, in Fig. 10, Fig. 11 and Fig. 12 are presented the histograms corresponding, respectively, to events occurring exclusively in P2, to events detected both in P2 and P1 and to events occurring only in P3. The relative contribution of each component is summarized in Tab. 2. Moreover, as indicated in Fig. 9, a fit was performed on the histogram corresponding to the total electron events.

Contribution	Events	Ratio (%)
Total events (P2 only, P2 and P1, P3 only)	11961	100.0%
P2 only	4098	34.3%
P2 and P1	3265	27.3%
P3 only	4598	38.4%

Table 2: Total number of events in the histogram including P2 only, P2 and P1, P3 only, with the relative contributions of each component. Percentages are computed with respect to the total number of entries.

The fit was performed to extract the parameters of interest, listed in Tab. 3, and compared

with the reference values indicated in Sec. 2. The fitting function used is:

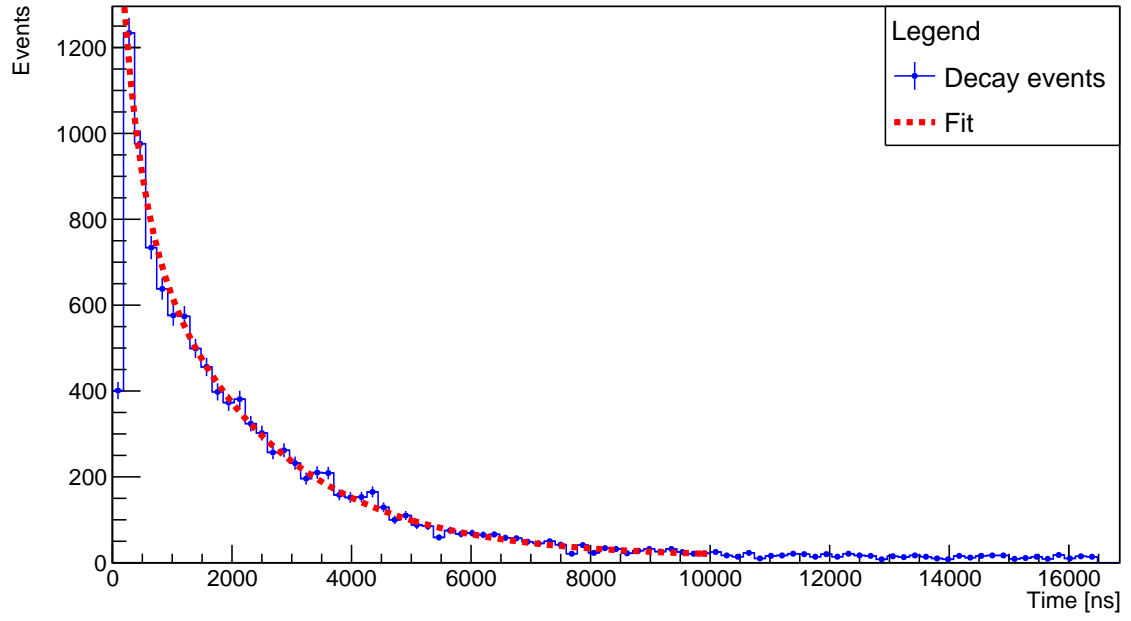
$$N(t) = N(\mu^+, 0)e^{-\frac{t}{\tau_0}} \left(1 + \frac{1}{R}e^{-\frac{t}{\tau_c}} \right) + b, \quad (11)$$

which is the muon decay law defined in Eq. 8, with an added constant term b to account for the accidental background. The maximum number of counts provided by the FPGA corresponds to $16 \mu\text{s}$, which explains why all data fall within the range $[0, 16000]$ ns. However, to perform the fit, a lower endpoint of 150 ns was selected based on the width of the P1 and P2 signals observed on the oscilloscope. Indeed, if the electron signal occurs within a time interval shorter than the duration of P1 and P2 after the trigger activation, the event is not registered by the FPGA. For this reason, the first few bins of the histograms in Fig. 9, Fig. 10, Fig. 11 and Fig. 12 contain very few events and were excluded from the analysis.

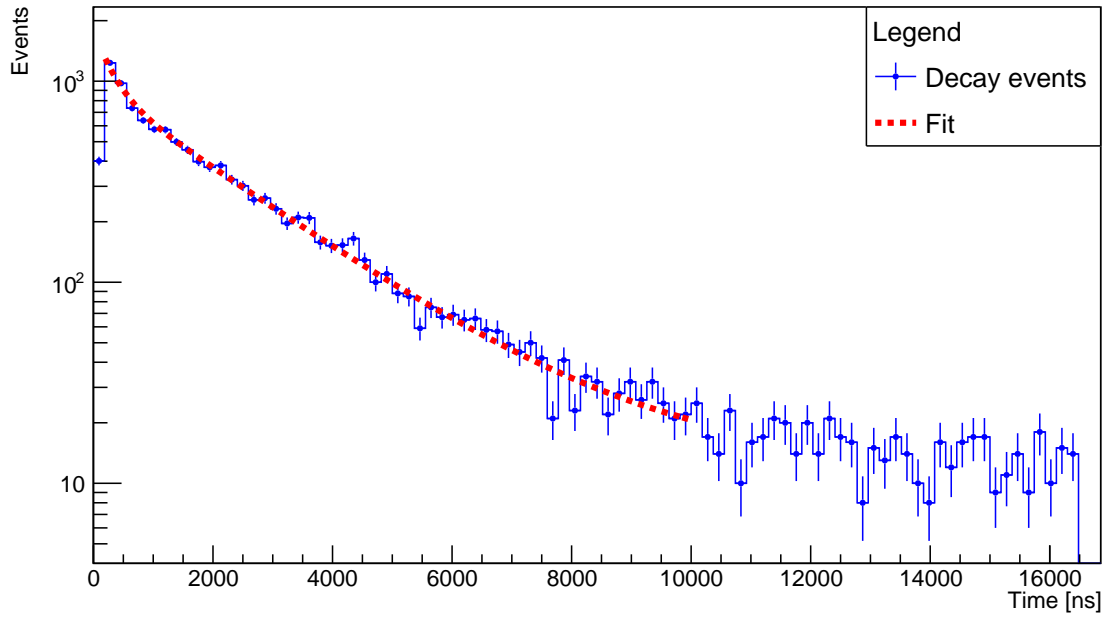
Estimated parameters	Value
$N_1(\mu^+, 0)$	(929 ± 29)
$\tau_{0,1}$	$(2.104 \pm 0.060) \mu\text{s}$
R_1	1.1 fixed value
$\tau_{c,1}$	$(0.343 \pm 0.044) \mu\text{s}$
Background (b_1)	(12.7 ± 2.3)
p-value	0.0053
χ^2/ν	1.59

Table 3: Fit results obtained with ROOT framework on the dataset measured with the setup including the iron absorber. The fit is performed on the histogram filled with the total events (P2 only, P2 and P1, P3 only).

The contribution of the two components to the μ^- mean lifetime, namely the capture rate τ_c and its pure decay τ_0 , is evident in Fig. 9, where the fitting function exhibits two slightly different behaviors. In particular, the short-time region (below 2000 ns) contains the steeper slope due to the faster decay component of nuclear capture, whereas in the region between 2000 ns and 6000 ns a more gradual slope appears, consistent with the exponential decay governed by τ_0 .



(a) Linear scale.



(b) Logarithmic scale.

Figure 9: Total electron events recorded in P2 only, P2 and P1, P3 only by the FPGA with the configuration shown in Fig. 1 and analyzed in $[150, 10000]$ ns range. The corresponding exponential fit is shown.

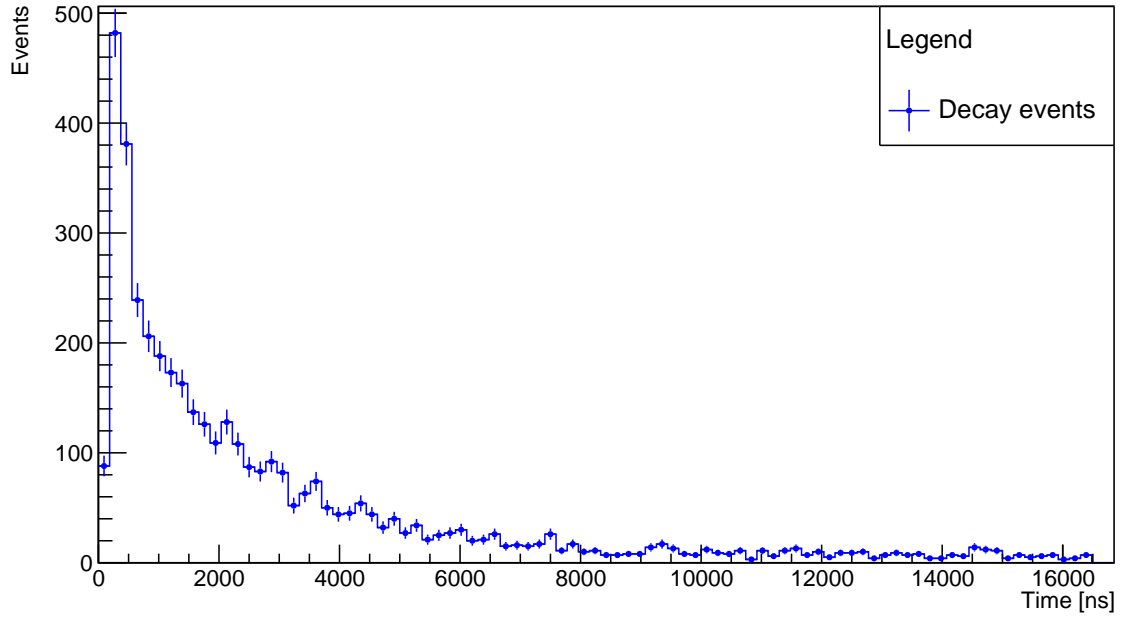


Figure 10: Electron events recorded only in P2 by the FPGA, with the configuration shown in Fig. 1.

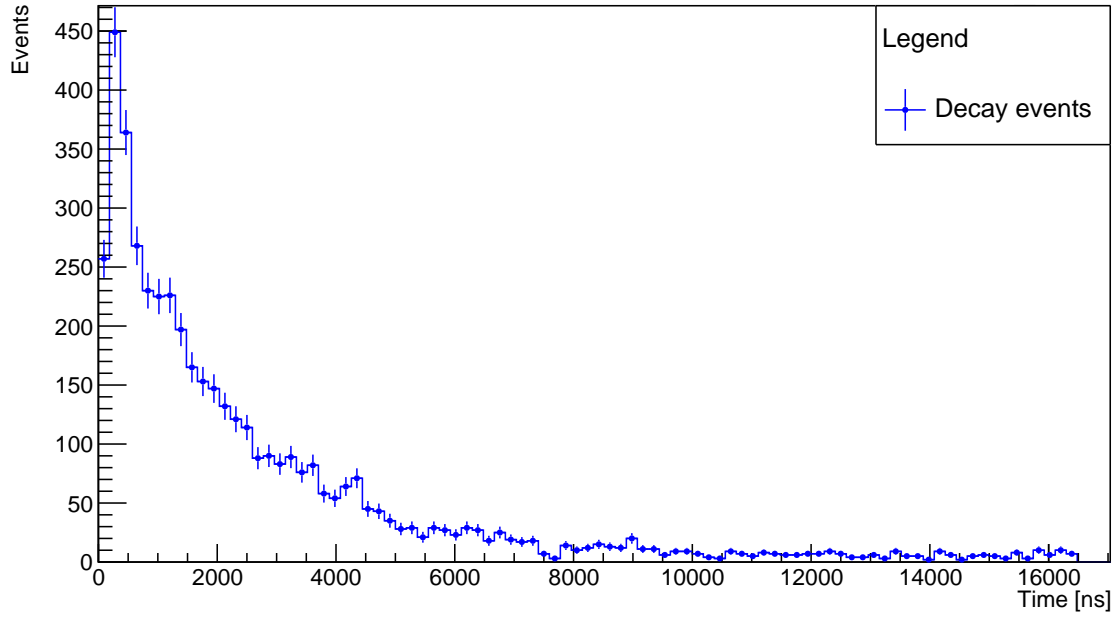


Figure 11: Electron events recorded both in P2 and P1 by the FPGA, with the configuration shown in Fig. 1.

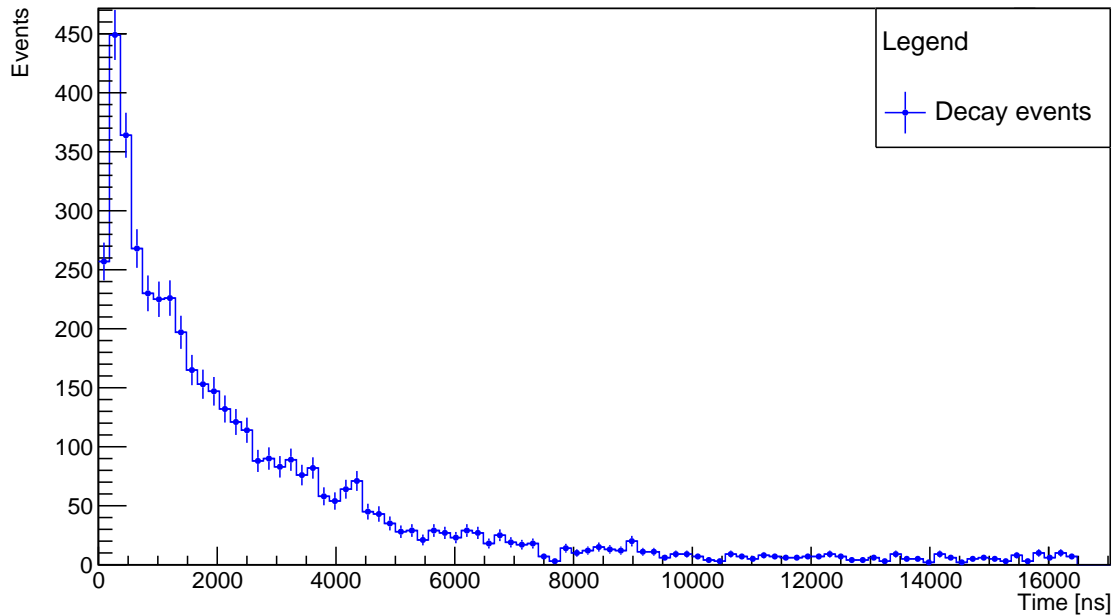


Figure 12: Electron events recorded in P3 by the FPGA, with the configuration shown in Fig. 1.

4.4 Muon decays occurring in iron

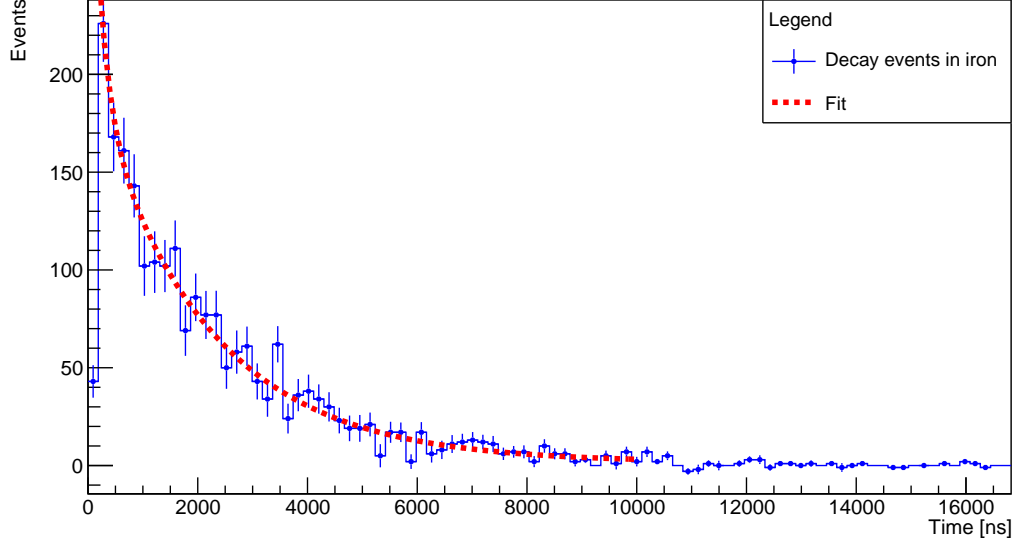
The dataset analyzed in Sec. 4.3 was produced through four different physical processes, all of which satisfy the trigger condition. In particular, referring to Fig. 1, most events (R_{Fe}) originate from muons decaying in iron, emitting an electron either upward (detected by P2 or P1 and P2) or downward (detected by P3). Additionally, some muons may decay within P2, also producing valid events ($R_{scintillator}$). Another class of events ($R_{acceptance}$) occurs when the muon does not decay in the iron plate but, due to the finite extension of the scintillators, it does not cross P3 and still activates the trigger. Lastly, an event can also be registered if, due to the inefficiency of P3, a muon that does not decay in the iron passes through it without being detected. This last case can however be neglected due to the high efficiency of the scintillator P3 in our setup. As a result, the total number of events measured with the configuration in Fig. 1 can be written as:

$$R_{TOT} = R_{Fe} + R_{scintillator} + R_{acceptance}. \quad (12)$$

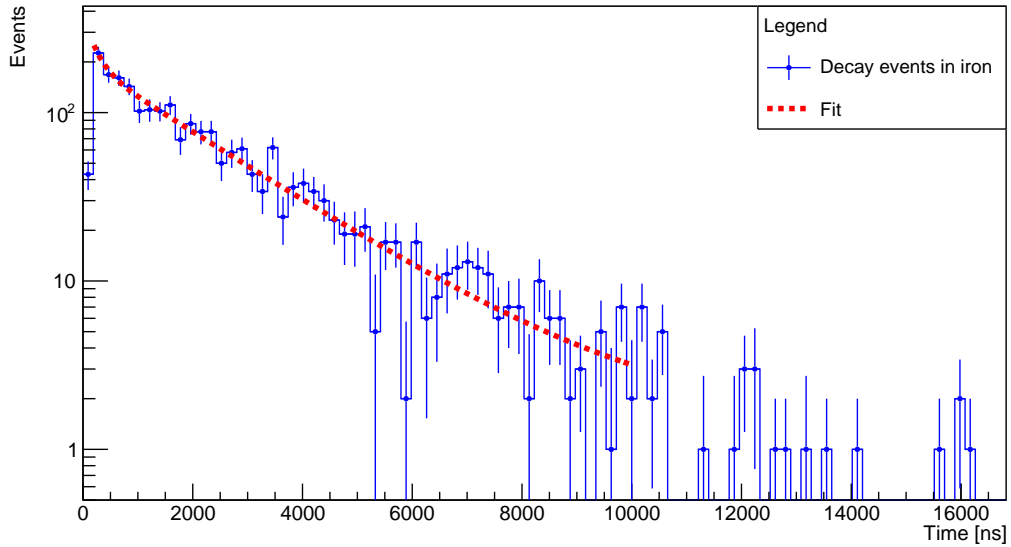
In contrast to the analysis performed using data acquired through the first configuration (Sec. 4.3), the setup described in Sec. 3.3 aimed for a more accurate estimation of the parameters of interest. Indeed, the removal of iron from the setup eliminates the contribution from muons decaying in iron (R_{Fe}), enabling an indirect estimate of their number. However, particular care must be taken into account to correctly interpret the differences between the two setup configurations. In particular, in the configuration with the iron absorber, the majority of events involving a signal in P1 and P2 originate from electrons emitted by muons decaying inside the iron or in P2 and going upward. Conversely, in the configuration without iron, any P1 and P2 signal must come from electrons produced by muons decaying in P2, which then travel upward. Therefore, since one of the aims of the experiment is to estimate the number of upward-going electrons produced by muon decay in iron (together with the number of muons captured in iron), it was necessary to select electron signals both in P1 and P2. This condition ensures a

meaningful subtraction between the datasets with and without iron.

With the above said, the estimate of muon events in iron was obtained by subtracting the histogram containing data acquired without the iron absorber (Sec. 3.3) from the one presented in Sec. 4.3.² The resulting difference histogram, which includes only events corresponding to muons producing signals in P1 and P2, is displayed in Fig. 13. A fit to this histogram enabled the extraction of the relevant parameters, which are summarized in Tab. 4.



(a) Linear scale.



(b) Logarithmic scale.

Figure 13: Difference of decay events obtained by subtracting data recorded with the configuration in Fig. 4 to the one in Fig. 1, both displaying P1 and P2 events. Data are analyzed in $[150, 10000]$ ns time range. The corresponding exponential fit is also shown.

²The datasets used in the subtraction were properly selected over the same time interval to ensure proper event normalization.

Estimated parameters	Value
$N_2(\mu^+, 0)$	(197 ± 17)
$\tau_{0,2}$	$(2.09 \pm 0.16) \mu s$
R_2	1.1 fixed value
$\tau_{c,2}$	$(0.231 \pm 0.097) \mu s$
Background (b_2)	(1.5 ± 1.2)
p-value	0.40
χ^2/ν	1.04

Table 4: Results of the fit, obtained with ROOT framework, performed over the histogram including only events corresponding to muons decaying in iron. The histogram is filled with the events which give a signal on both P1 and P2, and no signal on P3.

The histogram in Fig. 13, which includes only events corresponding to muons decaying in iron and traveling upward, contains 2237 entries. In comparison, the histogram in Fig. 11, representing all events in which a signal is provided in P1 and P2, contains 3265 entries. Consequently, the fraction of muons decaying in iron and emitting an upward electron relative to the total number of events is approximately 68.5%.

5 Conclusions

This experiment carries out the measurement of the muon lifetime, yielding $\tau_{0,1} = (2.104 \pm 0.060) \mu s$ for the dataset obtained with the iron absorber in the setup, plotted in Fig. 9, and $\tau_{0,2} = (2.09 \pm 0.16) \mu s$ for the one given by the subtraction between the previous dataset and the one collected without iron, shown in Fig. 13. While the first lifetime estimate is not compatible with the theoretical value within uncertainties, the second one shows compatibility. In addition, by fitting data shown in Fig. 9 and Fig. 13, estimates of the muon capture time in iron were obtained, providing respectively $\tau_{c,1} = (0.343 \pm 0.044) \mu s$ and $\tau_{c,2} = (0.231 \pm 0.097) \mu s$. Also in this case, only the second estimate is compatible with theoretical expectations, while the first is not.

Finally, an estimate of the number of muons decaying in iron and emitting an upward-going electron, together with the number of muons captured in iron, was made by comparing the number of events of the two data samples over the same time interval. The computation shows that 68.5% of the upgoing electrons decay in iron.

As shown in Tab. 3 and Tab. 4, the χ^2/ν value of the second fit is lower (1.04 vs 1.59), indicating that isolating muon decay events in iron not only yields a precise estimate of the number of muons that decay in iron, but also improves the agreement between data and the model function in Eq. 11. The p-value also improves significantly, increasing by two orders of magnitude from 0.0053 in the first fit to 0.40 in the second, confirming a substantially better goodness-of-fit. This is mainly due to the more refined dataset used in its determination, obtained by subtracting upgoing events not associated with muons decaying in iron. Moreover, parameters obtained from the second fit are characterized by larger uncertainties, summarized in Tab. 3 and Tab. 4. The lower precision of these parameters further contributes to reducing the χ^2/ν of the second fit, partly explaining its lower value when compared to the first fit.

Bibliography

- [1] D. M. Webber et al. *Measurement of the Positive Muon Lifetime and Determination of the Fermi Constant to Part-per-Million Precision*. 2010.
- [2] P. D. Group et al. “Review of Particle Physics”. In: *Progress of Theoretical and Experimental Physics* 2022.8 (Aug. 2022), p. 083C01.
- [3] R. Shah et al. *Charge ratio of cosmic ray muons in momentum range ~ 1 to 3 GeV/c*. 2024.